

pubs.acs.org/JACS Article

Magnetic Interactions in Substitutional Core-Doped Graphene Nanoribbons

Ethan Chi Ho Wen, Peter H. Jacobse, Jingwei Jiang, Ziyi Wang, Ryan D. McCurdy, Steven G. Louie, Michael F. Crommie, and Felix R. Fischer



Cite This: J. Am. Chem. Soc. 2022, 144, 13696-13703



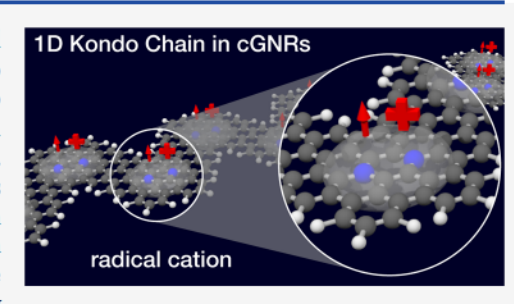
ACCESS

III Metrics & More

Article Recommendations

s Supporting Information

ABSTRACT: The design of a spin imbalance within the crystallographic unit cell of bottom-up engineered 1D graphene nanoribbons (GNRs) gives rise to nonzero magnetic moments within each cell. Here, we demonstrate the bottom-up assembly and spectroscopic characterization of a one-dimensional Kondo spin chain formed by a chevron-type GNR (cGNR) physisorbed on Au(111). Substitutional nitrogen core doping introduces a pair of low-lying occupied states per monomer within the semiconducting gap of cGNRs. Charging resulting from the interaction with the gold substrate quenches one electronic state for each monomer, leaving behind a 1D chain of radical cations commensurate with the unit cell of the ribbon. Scanning tunneling microscopy (STM) and spectroscopy



(STS) reveal the signature of a Kondo resonance emerging from the interaction of S = 1/2 spin centers in each monomer core with itinerant electrons in the Au substrate. STM tip lift-off experiments locally reduce the effective screening of the unpaired radical cation being lifted, revealing a robust exchange coupling between neighboring spin centers. First-principles DFT-LSDA calculations support the presence of magnetic moments in the core of this GNR when it is placed on Au.

INTRODUCTION

Magnetic ordering of π -electron spins in bottom-up engineered low-dimensional carbon nanomaterials makes them appealing candidates for applications in spintronic and quantum information processing. The emergence of magnetically ordered phases in all-carbon graphene nanostructures depends on the number and precise arrangement of atoms. Coulomb repulsion between electrons in a nanographene featuring a surplus of carbon atoms on sublattice A versus sublattice B will lead to a minimum of $\Delta N = N_A - N_B$ spin-polarized eigenstates at E = 0 eV (termed zero-modes) localized on the majority sublattice. This concept has been successfully employed to explore antiferromagnetic ordering in molecular structures, e.g., the Clar goblet,² rhombenes,³ zethrenes,⁴⁻⁷ and the family of triangulenes, 8-15 but the underlying principle can readily be expanded to substitutional heteroatom doping. 16 For instance, substitution of trigonal planar C-atoms with Natoms along the backbone of GNRs introduces a single surplus π -electron per dopant, which can give rise to local unpaired spin states in custom-tailored GNRs.

Here, we report the design, on-surface synthesis, and electronic characterization of one-dimensional (1D) S=1/2 spin chains emerging from charge transfer between nitrogen core-doped N₂-cGNRs and the underlying growth substrate. Rather than adopting an unfavorable $[4n\pi]$ electron configuration $(n \in \mathbb{N})$, each diazahexabenzocoronene subunit along the backbone of N₂-cGNRs donates a single electron to the Au substrate leaving a chain of highly localized radical cations

behind. While the positive charges lining the backbone of N_2^+ -cGNRs are effectively screened by image charges in the Au substrate, at cryogenic temperatures the unpaired electron spins along the ribbon are exchange-coupled to itinerant electrons in the underlying Au via the Kondo effect. The intraribbon coupling of adjacent S=1/2 spins was found to be $J_{\rm eff}=5$ meV using a combination of cryogenic inelastic tunneling spectroscopy (IETS) and single GNR lift-off through-conductance experiments. Our experimental results are consistent with first-principles calculations that imply ferromagnetic coupling between localized electron spin states along the backbone of isolated N_2^+ -cGNRs.

■ RESULTS AND DISCUSSION

Design and Synthesis of Molecular Precursors for N₂-cGNRs. Synthetic access to nitrogen core-doped cGNRs is facilitated by an on-surface thermal cyclodehydrogenation reaction that gives rise to covalent C–N bonds, as described in our recent reports. A key ingredient to this approach is the design of a molecular precursor built around a pyrazine core. The 1,4-arrangement of N-atoms in the pyrazine ring has been

Received: April 25, 2022 Published: July 22, 2022





shown to reduce the activation barrier for C-N bond formation during the cyclodehydrogenation step.²⁰ Adapting this design to the molecular repeat unit of cGNRs inspired the development of 11,16-dibromo-1,8-diphenyltetrabenzo-[a,c,h,j] phenazine (1), the molecular precursor for N₂cGNRs depicted in Figure 1. Following surface-assisted radical

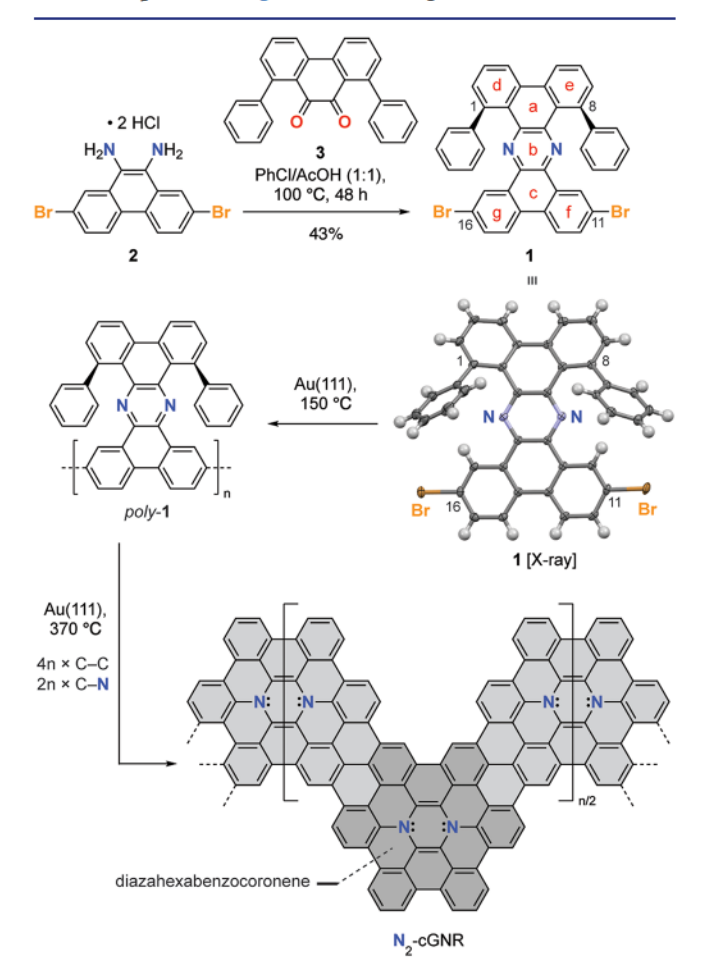


Figure 1. Bottom-up synthesis of N2-cGNRs from molecular precursor 1. Single X-ray crystal structure of 1. Thermal ellipsoids are drawn at the 50% probability level. Color coding: C (gray), N (blue), Br (orange), and H (white). Hydrogen atoms are placed at calculated positions. The diazahexabenzocoronene core in N2-cGNRs is highlighted in dark gray.

step-growth polymerization and thermal cyclodehydrogenation, N-atoms are fused to form the central core of each diazahexabenzocoronene repeating unit. The extended rigid carbon framework induces a trigonal planar geometry at the Natoms forcing the two valence electrons on nitrogen to share the p_z -orbital that contributes to the extended π -system of N_2 cGNRs.

The synthesis of the molecular precursor 1 is depicted in Figure 1. Imine condensation of 2,7-dibromophenanthrene-9,10-diamine dihydrochloride (2) with 1,8-diphenylphenanthrene-9,10-dione²² (3) yielded the tetrabenzo[a,c,h,j]phenazine core of 1. Single crystals suitable for X-ray diffraction were grown by slow diffusion of MeOH into a saturated solution of 1 in CH₂Cl₂. In the crystal, 1 adopts a C_s symmetric conformation. The dibenzo[f,h]quinoxaline core formed by rings b, c, g, and f (Figure 1) serving as the axis of polymerization during the surface-assisted growth of N2-cGNR

assumes a near-planar conformation reminiscent of the wellestablished family of cGNR precursors. The diphenylphenanthrene group formed by rings a, d, and e, however, adopts a saddle-like geometry (included angle between rings a and c $\sim 26^{\circ}$) placing the center of the two phenyl substituents at C1 and C8 1.5-1.6 Å above the plane of the dibenzo $[f_th]$ quinoxaline core, a key design element that ensures successful on-surface polymerization.

Surface-Assisted Growth of Core-Doped N₂-cGNR. Samples of N2-cGNRs were prepared following established cGNR growth protocols. Molecular precursor 1 was sublimed in ultrahigh vacuum (UHV) from a Knudsen cell evaporator onto a Au(111) surface held at 25 °C. Figure 2A shows a representative topographic STM image of monomer 1 selfassembled into a frustrated Kagome lattice commensurate with the Au(111) herringbone reconstruction. The preferred adsorption geometry of molecular precursor 1 shows two

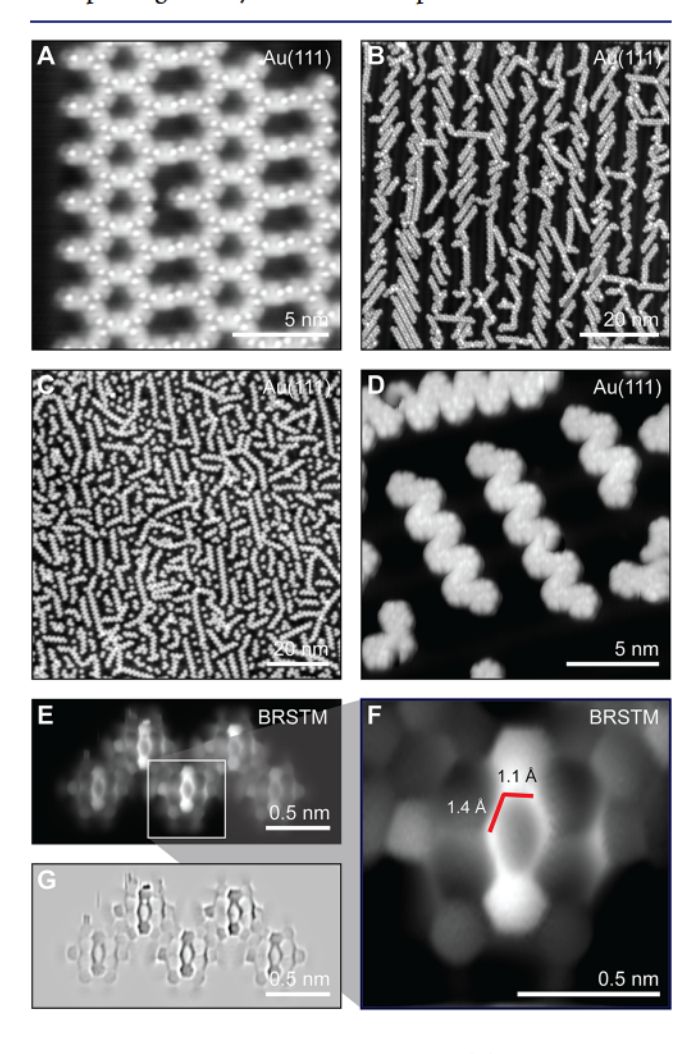


Figure 2. Bottom-up synthesis of N2-cGNRs. (A) STM topographic image of a self-assembled island of molecular precursor 1 on Au(111). (B) STM topographic image of intermediate polymer chains of poly-1 following thermal annealing to 150 °C. ($V_s = -1.8 \text{ V}$, $I_t = 80 \text{ pA}$). (C, D) STM topographic images of a sample of N2-cGNRs following annealing to 370 °C ($V_s = -1.8 \text{ V}$, $I_t = 100 \text{ pA}$). (E) Bond-resolved STM (BRSTM) image of a short segment of N_2 -cGNRs ($V_s = 0.1 \text{ V}$, $V_{\rm ac} = 30$ mV, f = 533 Hz, and $I_{\rm t} = 100$ pA). (F) BRSTM image of the region highlighted by a square in (E) showing the diazahexabenzocoronene core of a N2-cGNR subunit. (G) Laplace-filtered BRSTM image of the N_2 -cGNR segment shown in (E).

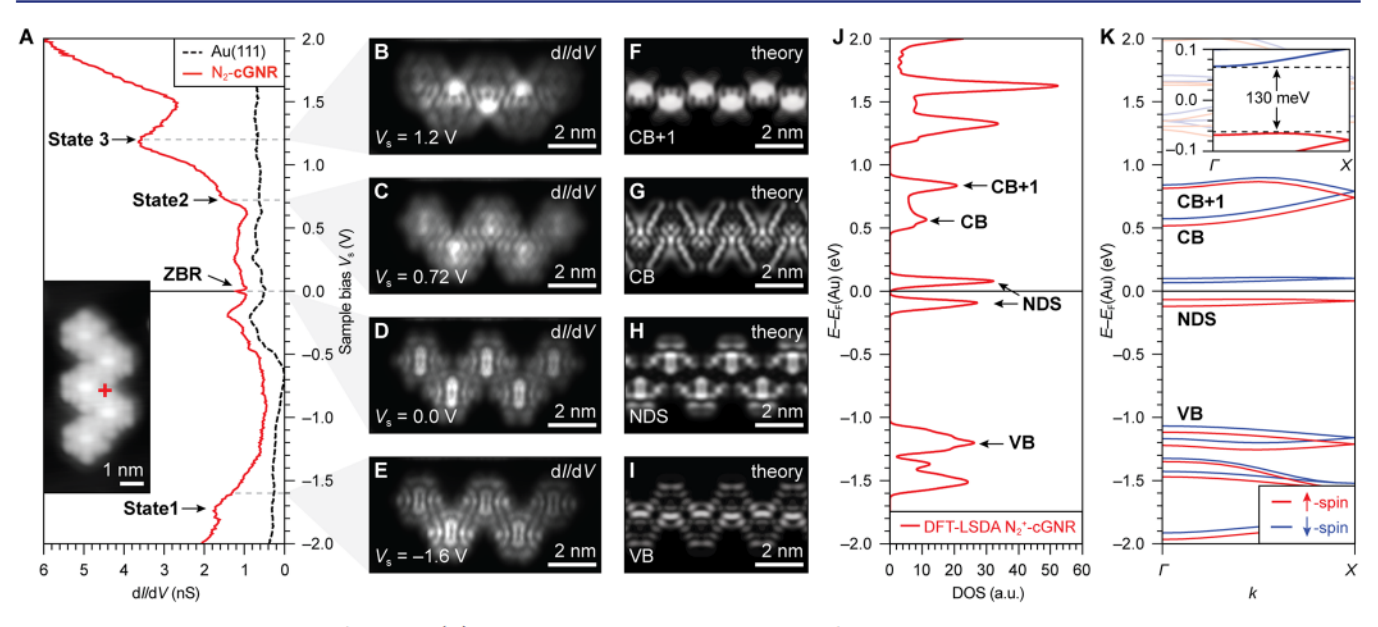


Figure 3. Electronic structure of N_2^+ -cGNRs. (A) STS dI/dV spectrum recorded on a N_2^+ -cGNR at the position marked by a red cross in the inset STM topographic image (spectroscopy: $V_{ac} = 4$ mV, f = 533 Hz; imaging: $V_s = 0.1$ V, $I_t = 200$ pA, CO-functionalized tip). (B–E) Constant height dI/dV maps recorded at the indicated biases ($V_{ac} = 30$ mV, f = 533 Hz, and CO-functionalized tip). (F–I) DFT-simulated LDOS maps of the CB +1, CB, NDS, and the VB of N_2^+ -cGNR. The maps are calculated at the band edge energies. (J) DFT-LSDA-calculated DOS of N_2^+ -cGNR. The N_2^+ -cGNR is doped with two holes per unit cell which contains two diazahexabenzocoronene cores (spectrum broadened by 30 meV Gaussian). Features associated with the CB+1, CB, NDS, and VB are indicated by arrows. (K) DFT-LSDA-calculated band structure of N_2^+ -cGNR. The inset shows the opening of an indirect band gap attributed to the Stoner magnetic instability.

characteristic bright spots flanking the center of each monomer unit (Supporting Information, Figure S1). This feature is consistent with the orientation of two phenyl substituents, attached to C1 and C8 in 1 (Figure 1), protruding above the plane of the molecule and is reminiscent of the saddle-like geometry adopted in the crystal lattice. Annealing the molecule-decorated surface at T_1 = 150 °C induces a radical step-growth polymerization that gives rise to extended polymer intermediates (poly-1, Figure 2B). A second annealing step at T₂ = 370 °C, required to ensure exhaustive cyclodehydrogenation, establishes the fully conjugated backbone of N2-cGNRs (Figure 2C,D). Topographic STM images reveal the characteristic pattern of extended chevron-type GNRs ranging in length from 15 to 25 nm (Supporting Information, Figure S2). Bondresolved STM (BRSTM) imaging with CO-functionalized tips (Figure 2E-G) confirms that the second annealing step reliably promotes the formation of four covalent C-C bonds and two C-N bonds per monomer that give rise to the diazahexabenzocoronene core of N2-cGNRs. The central phenazine ring in N2-cGNRs appears as a bright feature in low bias STM images. While the apparent bond lengths, C-N and C-C, 1.4 and 1.1 Å, respectively, are exaggerated by electrostatic interactions between the CO molecule attached to the apex of the STM tip and the local electron density of the sample,²³ the trend mirrors DFT-calculated bond length alternation induced to avoid local $[4n\pi]$ antiaromaticity.²⁴

Electronic Characterization of Core-Doped N_2 -cGNR. With the internal chemical bonding of N_2 -cGNRs resolved, we set out to characterize their electronic structure using scanning tunneling spectroscopy. Figure 3 shows a dI/dV point spectrum of N_2 -cGNRs recorded at the position highlighted by the red cross in the topographic STM image (Figure 3A, inset). Two features, a peak at $V_s = -1.7$ V, State 1, and a shoulder at $V_s = +0.7$ V, State 2, bracket the E_F . Besides a second prominent feature at larger positive bias, $V_s = +1.2$ V

(State 3), the dI/dV spectrum of N_2 -cGNRs shows a peak centered at $V_s = 0.0$ V. The intensity of this zero-bias resonance (ZBR) is largest when the STM tip is positioned above the center of a diazahexabenzocoronene subunit and decays radially in all directions. dI/dV maps recorded at $V_s =$ 0.0 V (Figure 3D) show that the density of states (DOS) is localized primarily on the central phenazine core of each monomer subunit consistent with the theoretically predicted projection of the LDOS of the nitrogen dopant state (NDS) (Figure 3H). While the assignment of State 1 to the valence band (VB) edge is tempting, 25,26 the corresponding dI/dV map recorded at $V_s = -1.6 \text{ V}$ (Figure 3E) shows patterns reminiscent of the ZBR rather than the predicted LDOS associated with the VB (Figure 3I). The similarity between dI/dV maps recorded at $V_s = -1.6 \text{ V}$ and $V_s = 0.0 \text{ V}$ suggests that State 1 can be attributed to the positive ion resonance (PIR) resulting from resonant tunneling of holes into the same orbital imaged in the ZBR. The position of the corresponding negative ion resonance (NIR) could not be identified in the spectroscopy. State 2 at $V_s = +0.7$ V shows patterns that mirror the predicted LDOS associated with the CB (Figure 3G). At higher bias, $V_s = +1.2 \text{ V}$ (State 3), the dI/dV map (Figure 3B) displays the characteristic signature of the CB + 1 state (Figure 3F). The energy and spatial localization of the ZBR coincides with the anticipated position of NDS (Supporting Information, Figure S3), but the unusual line shape and exceptionally narrow width suggest an alternative explanation involving the Kondo effect.

Figure 4A shows a dI/dV point spectrum recorded over a narrow bias window (± 50 meV) at the position marked in the inset. The most prominent feature is a peak centered at zero bias, which can be fit to a Frota line shape 27,28

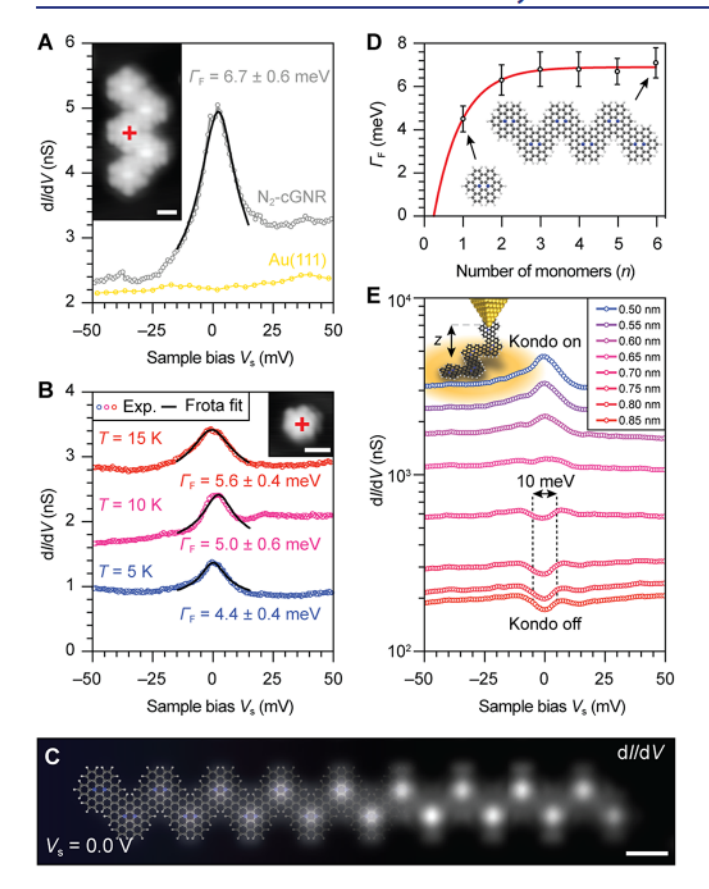


Figure 4. Kondo resonance in N_2^+ -cGNRs. (A) dI/dV spectrum recorded on a N_2^+ -cGNR at the position marked in the inset. Γ_F is the Frota parameter (spectroscopy: $V_{\rm ac}=1$ mV, f=533 Hz; imaging: $V_{\rm s}=0.1$ V, $I_{\rm t}=200$ pA). (B) Variable temperature dI/dV spectra recorded on a diazahexabenzocornonene monomer at the position marked in the inset (spectra are vertically offset by 1 nS for clarity). (C) Constant height dI/dV map of an octadecamer N_2^+ -cGNR recorded with an unfunctionalized STM tip at $V_{\rm s}=0.0$ V showing the spatial density variations of the ZBR associated with the 1D Kondo chain. A structural model of N_2 -cGNR is overlaid on the left side of the ribbon. (D) Evolution of Γ_F as a function of the N_2^+ -cGNR length. (E) STS lift-off experiment performed on a heptamer N_2^+ -cGNR. The color gradient indicates the apparent z-height of the STM tip above the surface. Scale bars: 1 nm.

$$T_{\rm F}(\varepsilon) = T_0 - A \cdot Re \left[e^{iq} \sqrt{\frac{i\Gamma_{\rm F}}{\varepsilon - \varepsilon_0 + i\Gamma_{\rm F}}} \right] \tag{1}$$

where T_0 is the background tunneling signal, A is the amplitude and q is the symmetry factor of the Frota function, ε_0 is the center of the resonance, and Γ_F is the Frota parameter related to the half-width at half-maximum: HWHM $\sim 2.54\Gamma_{\rm F}$. The position of a ZBR at $V_s = 0.0$ V, the unusually narrow width $\Gamma_{\rm F}$ = 6.7 \pm 0.6 meV at T = 5 K, and the Frota line shape are all suggestive of a Kondo resonance arising from the scattering of conduction electrons in the Au substrate by a localized unpaired electron spin in the GNR. 29-35 To further corroborate the assignment of the ZBR to a magnetic exchange interaction, we performed temperature-dependent STS.3 Figure 4B shows the expected broadening of the ZBR resonance from $\Gamma_{\rm F}$ = 4.4 \pm 0.4 meV, $\Gamma_{\rm F}$ = 5.0 \pm 0.6 meV, to $\Gamma_{\rm F}$ = 5.6 \pm 0.4 meV as the temperature is increased from T= 5 K, T = 10 K, to T = 15 K, respectively (we have deconvoluted the effect of thermal broadening in our fitting procedure to obtain these values). The observed effect is much greater than the thermal broadening of the Fermi-Dirac distribution function alone and is expected for a Kondo resonance.

dI/dV maps recorded at zero bias (Figure 4C) reveal that the Kondo states form a 1D lattice along the backbone of N₂cGNRs that is superimposable with the number and position of diazahexabenzocoronene cores in a given ribbon. The periodicity suggests that each subunit hosts unpaired electron spin density resulting from charge transfer between the ribbon and the Au substrate, leaving behind a chain of diazahexabenzocoronene radical cations along the backbone of the ribbon. We herein label this heavily p-doped state with the prefix N2+. While the Kondo screening of highly localized radical cation states in N2+-cGNRs by itinerant electrons in the underlying Au precludes the direct observation of intraribbon spin excitations by IETS, some interaction between adjacent spins, despite their Kondo screening, is suggested by the broadening of the Kondo resonance as a function of ribbon length. 34,37,38 The average $\Gamma_{\rm F}$ of the Kondo peaks recorded for a series of N_2^+ -cGNRs ranging from the monomer (n = 1) to the hexamer (n = 6) is depicted in Figure 4D. Γ_F increases by > 40% when moving from the isolated monomer to the dimer (n= 2) or trimer (n = 3) before stabilizing at $\Gamma_F \sim 6.8$ eV for $n \ge 1$ 4. Other possible explanations for this Kondo peak broadening include variations in the adsorption height, 39,40 the spatial position of the tip relative to the Kondo orbital, 41,42 and the energetic alignment of the NDS relative to the Fermi energy. We rule out possible Kondo width variations due to tip positioning by recording the dI/dV on top of the center of the pyrazine ring every time, averaging over multiple spectra and over multiple N2+-cGNRs. The adsorption height of N2+cGNRs was found to be identical to that of the single monomer ($z = 2.5 \pm 0.1$ Å when scanning over the pyrazine ring and $z = 2.3 \pm 0.1$ Å when scanning around the pyrazine ring). While we cannot completely rule out the possibility that the energetic alignment of the NDS could cause some width variations in the Kondo resonance, we will show later that we can resolve spin-flip excitations when the Kondo screening of N2⁺-cGNRs is reduced. This supports our hypothesis that nonzero exchange coupling between neighboring S = 1/2 spin centers broadens the Kondo peak for N_2^+ -cGNRs.

First-Principles Electronic Structure Calculation. We further explored the band structure of charged N2+-cGNRs using ab initio density functional theory (DFT). We herein have to rely on an approximation as the Fermi levels of N2cGNRs and Au(111), when measured with respect to the vacuum level, are misaligned. N₂-cGNRs placed on a Au(111) substrate will experience doping until the Fermi energy of N2cGNRs matches that of the underlying Au. The effective charge transfer can be estimated by calculating the Fermi level of isolated charged N2-cGNRs with respect to the vacuum level and then comparing it to the Fermi level of Au, also referenced to vacuum. We find that the N2-cGNR Fermi level aligns with that of Au when it is doped with two holes (total charge is +2) per unit cell (it becomes the N2+-cGNR since there are two pairs of nitrogen atoms per unit cell). A secondary dipole effect between the Au surface and N2+-cGNR can be ignored in this approximation. Figure 3J,K shows the theoretical DOS and the band structure of N2+-cGNRs calculated using the local spin density approximation (LSDA). Characteristic peaks associated with the bulk VB and CB edges can be seen at -1.10 eV and +0.55 eV, respectively. The most prominent features in the

DOS however are two in-gappeaks bracketing $E_{\rm F}$. The signatures emerge from two half-filled flat bands ($\Delta E < 50$ meV) splitted by magnetic interaction associated with the nitrogen dopant states (NDS) (Supporting Information, Figure S3). Figure 3H shows a projection of the LDOS associated with the NDS maps onto the precise position of phenazine cores along the backbone of N₂-cGNRs. The calculated spatial distribution of the NDS is consistent with experimental dI/dVmaps recorded at zero bias. The exceptionally high DOS at $E_{\rm F}$ introduced by nitrogen core doping makes isolated N2+cGNRs highly susceptible to metal-insulator phase transitions described by the Mott theory or the Stoner magnetic instability. 44 Figure 3K shows that N2+-cGNRs in fact undergo a magnetic phase transition that opens a sizeable gap of $\Delta E_{\rm LSDA}$ = 130 meV around E_F. The NDS split into a pair of spinpolarized bands with up-spin characters that come to rest below $E_{\rm F}$ and a pair of unoccupied bands with down-spin characters. Theory predicts that the ferromagnetically ordered ground state in N2+-cGNRs is preferred by 63 meV per unit cell over the nonmagnetic ground state.

Lift-Off and Through-Conductance Experiments. To access the magnetic interactions between S = 1/2 radical cations along the backbone of N2+-cGNRs, we performed liftoff experiments. Here, the STM tip is attached to one end of the ribbon and the differential through-conductance is recorded as the tip is incrementally retracted along the z-axis lifting one end of the ribbon from the surface. Figure 4E shows the evolution of the dI/dV spectrum as a function of the apparent height z for a heptamer N2+-cGNR. At small z, the Kondo resonance dominates the dI/dV spectrum, indicating that the S = 1/2 spins in the ribbon are Kondo-screened by itinerant electrons in the Au substrate. As the tip-surface distance increases ($z \sim 0.7$ nm in Figure 4E), the Kondo peak vanishes, giving way to two low-energy spectral features centered at $V_s = \pm 5.0$ mV. While the apparent STM tip height z associated with the spectral transition varies between lift-off experiments (due to unpredictability in the attachment geometry to the tip), the exact position of the two symmetric conductance steps is independent of the length or which end of the ribbon is lifted from the surface (Supporting Information, Figure S4). No signs are observed during lift-off experiments (such as a resonance shifting through E_F), that indicate back electron transfer from the Au to restore the closed-shell electron configuration of a neutral N2-cGNR.⁴⁵ This behavior can be explained by progressive weakening of the Kondo screening of the two S = 1/2 spin centers on adjacent radical cation subunits near the tip as the N2+-cGNR is lifted. At some point, the exchange interaction between the two adjacent spins (J_{eff}) dominates over the weakened Kondo effect and the two spins lock into either a net singlet or triplet ground state (the ferromagnetic ground state of isolated N2+-cGNRs would suggest a triplet ground state). IETS is then able to probe J_{eff} through spin-flip excitations of the coupled spin centers. The dip in the dI/dV for $z \ge 0.7$ nm can then be interpreted as the onset of spin-flip excitations at a threshold indicating $J_{\rm eff} \sim 5$ meV. This exchange coupling may also explain the lengthdependent broadening of the Kondo resonance seen in Figure $4D.^{32}$

CONCLUSIONS

We have demonstrated the rational bottom-up synthesis of an S = 1/2 chain in N₂-cGNR adsorbed onto Au(111). Our strategy utilizes the design of an energetically unfavorable

 $[4n\pi]$ electron configuration inside a GNR unit cell through nitrogen core doping. Partial charge transfer between N2cGNRs and the metal surface establishes the required electron configuration that gives rise to a spin imbalance. The resulting N_2^+ -cGNR behaves as an S = 1/2 chain where each diazahexabenzocoronene repeating subunit hosts an unpaired spin that interacts both with its neighboring spins and the metal surface. The exchange interaction between adjacent S =1/2 subunits was studied via GNR lift-off through-conductance experiments. First-principles DFT-LSDA calculations corroborate the strong hole doping of N2+-cGNRs on Au(111) required to generate the S = 1/2 chain and predict a ferromagnetic ground state in the absence of Kondo screening. Our results provide a blueprint for designing 1D spin systems in bottom-up synthesized GNRs, providing a new opportunity for exploring nontrivial spin physics and developing future spintronic devices.

■ EXPERIMENTAL SECTION

Materials and Instrumentation. Unless otherwise stated, all manipulations of air- and/or moisture-sensitive compounds were carried out in oven-dried glassware, under an atmosphere of N2. All solvents and reagents were purchased from Alfa Aesar, Spectrum Chemicals, Acros Organics, TCI America, and Sigma-Aldrich and were used as received unless otherwise noted. Organic solvents were dried by passing through a column of alumina and were degassed by vigorous bubbling of N2 through the solvent for 20 min. Flash column chromatography was performed on SiliCycle silica gel (particle size 40-63 μm). Thin-layer chromatography was carried out using SiliCycle silica gel 60 Å F-254 precoated plates (0.25 mm thick) and visualized by UV absorption. All ¹H and ¹³C(¹H) NMR spectra were recorded on Bruker AV-600, MHz spectrometers and are referenced to residual solvent peaks (CDCl₃ ¹H NMR = 7.26 ppm, ¹³C(¹H) NMR = 77.16 ppm). ESI mass spectrometry was performed on a Finnigan LTQFT (Thermo) spectrometer in positive ionization mode. X-ray crystallography was performed on a Rigaku XtaLAB P200 equipped with a MicroMax 007HF dual-source rotating anode and a Pilatus 200 K hybrid pixel array detector. Data were collected using Mo K α ($\lambda = 0.71073$ Å) radiation. Crystals were kept at 100 K throughout the collection using an Oxford Cryostream 700 for 1. Data collection was performed with CrysAlisPro. 46 Data was processed with CrysAlisPro and includes a multiscan absorption correction applied using the SCALE3 ABSPACK scaling algorithm within CrysAlisPro. Crystallographic data was solved with ShelXT, refined with ShelXL, and finalized in Olex1.5. 3 was synthesized following literature procedures.22

11,16-Dibromo-1,8-diphenyltetrabenzo[a,c,h,j]phenazine (1). A 250 mL two-neck round-bottom flask was charged with 2,7dibromophenanthrene-9,10-dione (2.50 g, 6.83 mmol), H₂NOH·HCl (2.37 g, 34.2 mmol), and pyridine (3 mL) in EtOH (70 mL). A reflux condenser was attached, and the reaction mixture was stirred for 6 h at 80 °C. The reaction mixture was concentrated on a rotary evaporator (1/2 v/v) and cooled to 24 °C. The yellow precipitate was filtered, washed thoroughly with cold EtOH, and dried under vacuum. Crude 9,10-N,N'-dihydroxyphenanthrene-9,10-diimine (2.41 g) was used without further purification. A 100 mL two-neck round-bottom flask was charged with 9,10-N,N'-dihydroxyphenanthrene-9,10diimine (0.200 g, 0.505 mmol) in EtOH (25 mL). SnCl₂ (0.940 g, 5.05 mmol) was dissolved in concentrated HCl (4 mL) and added in portions to the reaction mixture. A reflux condenser was attached, and the reaction mixture was stirred for 8 h at 80 °C. The reaction mixture was cooled to 24 °C. The precipitate was filtered, washed with H2O and cold EtOH (10 mL), and dried under vacuum. Crude 2,7dibromo-9,10-dihydrophenanthrene-9,10-diamine dihydrochloride 2 (0.149 g) was used without further purification. A 25 mL Schlenk flask was charged with 2 (0.083 g, 0.19 mmol) and 3 (0.045 g, 0.12 mmol) in PhCl (4 mL) and AcOH (4 mL). The reaction mixture was degassed by sparging with N2 for 20 min and stirred under a N2

atmosphere for 48 h at 100 °C. The reaction mixture was concentrated, diluted with saturated aqueous NaHCO₃ (50 mL), and extracted with CHCl₃ (100 mL). The combined organic phases were washed with H₂O (50 mL), saturated aqueous NaCl (50 mL), dried over MgSO₄, and concentrated on a rotary evaporator. Column chromatography (SiO₂; 1:1 CHCl₃/toluene) yielded 1 (0.036 g, 0.05 mmol, 43%) as a yellow solid. ¹H NMR (600 MHz, CDCl₃) δ = 8.70 (d, J = 8.2 Hz, 2H), 8.11 (d, J = 8.7 Hz, 2H), 7.84 (t, J = 8.1 Hz, 2H), 7.68 (dd, J = 7.3, 1.1 Hz, 2H), 7.65 (dd, J = 8.6, 2.2 Hz, 2H), 7.54—7.48 (m, 12H) ppm; ¹³C{¹H} NMR (151 MHz, CDCl₃) δ = 145.7, 143.0, 142.4, 137.1, 133.8, 132.8, 132.7, 131.7, 129.5, 129.4, 129.3, 128.4, 128.3, 128.0, 127.6, 123.9, 122.8, 122.7 ppm (two ¹³C signals are masked by overlapping peaks); HRMS (EI-TOF) m/z: $[C_{40}H_{22}Br_2N_2]^+$ calcd. $[C_{40}H_{22}Br_2N_2]^+$ 690.0129; found 690.0127.

 N_2 -cGNR Growth on Au(111) Surfaces. N_2 -cGNRs were grown on Au(111)/mica films under UHV conditions. Atomically clean Au(111) surfaces were prepared through iterative Ar⁺ sputter/anneal cycles. Submonolayer coverage of 1 on atomically clean Au(111) was obtained by sublimation at crucible temperatures of 410 K using a home-built Knudsen cell evaporator. After deposition, the surface temperature was slowly ramped (\leq 2 K min⁻¹) to 425 K and held at this temperature for 30 min to induce radical step-growth polymerization and then ramped up slowly (\leq 2 K min⁻¹) to 640 K and held for 30 min to induce cyclodehydrogenation.

Scanning Tunneling Microscopy and Spectroscopy. All STM experiments were performed using a commercial Createc LT-STM operating at T=4 K using chemically etched tungsten STM tips. $\mathrm{d}I/\mathrm{d}V$ measurements were recorded using a lock-in amplifier with a modulation frequency of f=533 Hz and a modulation amplitude of $V_{\mathrm{ac}}=1.0-4.0$ mV. $\mathrm{d}I/\mathrm{d}V$ point spectra and $\mathrm{d}I/\mathrm{d}V$ maps were recorded at a constant height, under open feedback loop conditions.

Calculations. First-principles DFT calculations in the LDA and LSDA approximations were implemented using the Quantum Espresso package. The used norm-conserving pseudopotentials with a 60 Ry energy cutoff and 0.005 Ry Gaussian broadening. To ensure the accuracy of our results, a sufficiently large vacuum region of ~15 Å was included in the supercell calculation. All of the dangling bonds at the edge of the carbon skeleton were terminated with Hatoms. The structures were first fully relaxed until all components of the force were smaller than 0.01 eV/Å.

ASSOCIATED CONTENT

Supporting Information

The Supporting Information is available free of charge at https://pubs.acs.org/doi/10.1021/jacs.2c04432.

Synthetic procedures and characterization of 1; X-ray crystal structure data for 1 [CCDC 2133137] (PDF)

Accession Codes

CCDC 2133137 contains the supplementary crystallographic data for this paper. These data can be obtained free of charge via www.ccdc.cam.ac.uk/data_request/cif, or by emailing data_request@ccdc.cam.ac.uk, or by contacting The Cambridge Crystallographic Data Centre, 12 Union Road, Cambridge CB2 1EZ, UK; fax: +44 1223 336033.

CCDC 2133137 contains the supplementary crystallographic data for 1. The data can be obtained free of charge via www.ccdc.cam.ac.uk/data_request/cif, by emailing data_request@ccdc.cam.ac.uk, or by contacting The Cambridge Crystallographic Data Centre, 12 Union Road, Cambridge CB2 1EZ, U.K.; Fax: +44 1223 336033.

AUTHOR INFORMATION

Corresponding Authors

Steven G. Louie – Department of Physics, University of California, Berkeley, California 94720, United States; Materials Sciences Division, Lawrence Berkeley National Laboratory, Berkeley, California 94720, United States; orcid.org/0000-0003-0622-0170; Email: sglouie@berkeley.edu

Michael F. Crommie — Department of Physics, University of California, Berkeley, California 94720, United States; Materials Sciences Division, Lawrence Berkeley National Laboratory, Berkeley, California 94720, United States; Kavli Energy NanoSciences Institute at the University of California Berkeley and the Lawrence Berkeley National Laboratory, Berkeley, California 94720, United States; orcid.org/0000-0001-8246-3444; Email: crommie@berkeley.edu

Felix R. Fischer — Department of Chemistry, University of California, Berkeley, California 94720, United States; Materials Sciences Division, Lawrence Berkeley National Laboratory, Berkeley, California 94720, United States; Kavli Energy NanoSciences Institute at the University of California Berkeley and the Lawrence Berkeley National Laboratory, Berkeley, California 94720, United States; orcid.org/0000-0003-4723-3111; Email: ffischer@berkeley.edu

Authors

Ethan Chi Ho Wen — Department of Chemistry, University of California, Berkeley, California 94720, United States

Peter H. Jacobse — Department of Physics, University of California, Berkeley, California 94720, United States

Jingwei Jiang — Department of Physics, University of California, Berkeley, California 94720, United States; Materials Sciences Division, Lawrence Berkeley National Laboratory, Berkeley, California 94720, United States;

orcid.org/0000-0002-0949-4401

Ziyi Wang — Department of Physics, University of California, Berkeley, California 94720, United States; orcid.org/ 0000-0003-1049-5038

Ryan D. McCurdy — Department of Chemistry, University of California, Berkeley, California 94720, United States;
orcid.org/0000-0001-7319-4836

Complete contact information is available at: https://pubs.acs.org/10.1021/jacs.2c04432

Author Contributions

¹E.C.H.W., P.H.J., J.J. contributed equally to this work. All authors have given approval to the final version of the manuscript.

Notes

The authors declare no competing financial interest.

ACKNOWLEDGMENTS

This work was primarily funded by the US Department of Energy (DOE), Office of Science, Basic Energy Sciences (BES), Materials Sciences and Engineering Division under contract DE-AC02-05-CH11231 (Nanomachine program KC1203) (molecular design, surface characterization, *ab initio* calculations). The research was also supported by the Office of Naval Research under awards N00014-19-1-2503 (molecular characterization), N00014-19-1-2596 (STM lift-off measurements), and the National Science Foundation under Grant No. DMR-1839098 (image analysis). STM instruments are supported by the Office of Naval Research under award N00014-20-1-2824. This research used resources of the National Energy Research Scientific Computing Center (NERSC) a US Department of Energy Office of Science User Facility operated under Contract No. DE-AC02-05-

CH11231. Computational resources were also provided by the National Science Foundation through XSEDE resources at the NICS. E.C.H.W. acknowledges support from the Croucher Foundation through a Croucher Scholarship for Doctoral Study. P.H.J. acknowledges fellowship support from the Dutch Research Council through the Rubicon Award (019.182EN.18). The authors thank the College of Chemistry (CoC) for use of resources at their NMR and small molecule X-ray crystallography facility, and the authors thank their staff for assistance. Instruments in CoC-NMR facility are supported in part by NIH S10-OD024998. Instruments in CoC-X-ray facility are supported in part by NIH S10-RR027172.

REFERENCES

- (1) Yazyev, O. V. Emergence of magnetism in graphene materials and nanostructures. *Rep. Prog. Phys.* 2010, 73, No. 056501.
- (2) Mishra, S.; Beyer, D.; Eimre, K.; Kezilebieke, S.; Berger, R.; Groning, O.; Pignedoli, C. A.; Muellen, K.; Liljeroth, P.; Ruffieux, P.; Feng, X. L.; Fasel, R. Topological frustration induces unconventional magnetism in a nanographene. *Nat. Nanotechnol.* 2020, 15, 22–28.
- (3) Mishra, S.; Yao, X. L.; Chen, Q.; Eimre, K.; Groning, O.; Ortiz, R.; Di Giovannantonio, M.; Sancho-Garcia, J. C.; Fernandez-Rossier, J.; Pignedoli, C. A.; Mullen, K.; Ruffieux, P.; Narita, A.; Fasel, R. Large magnetic exchange coupling in rhombus-shaped nanographenes with zigzag periphery. *Nat. Chem.* 2021, 13, 581–586.
- (4) Zeng, W. D.; Gopalakrishna, T. Y.; Phan, H.; Tanaka, T.; Herng, T. S.; Ding, J.; Osuka, A.; Wu, J. S. Superoctazethrene: An Open-Shell Graphene-like Molecule Possessing Large Diradical Character but Still with Reasonable Stability. *J. Am. Chem. Soc.* 2018, 140, 14054–14058.
- (5) Mishra, S.; Melidonie, J.; Eimre, K.; Obermann, S.; Groning, O.; Pignedoli, C. A.; Ruffieux, P.; Feng, X. L.; Fasel, R. On-surface synthesis of super-heptazethrene. *Chem. Commun.* **2020**, *56*, 7467–7470.
- (6) Turco, E.; Mishra, S.; Melidonie, J.; Eimre, K.; Obermann, S.; Pignedoli, C. A.; Fasel, R.; Feng, X. L.; Ruffieux, P. On-Surface Synthesis and Characterization of Super-nonazethrene. *J. Phys. Chem. Lett.* 2021, 12, 8314–8319.
- (7) Huang, R.; Phan, H.; Herng, T. S.; Hu, P.; Zeng, W. D.; Dong, S. Q.; Das, S.; Shen, Y. J.; Ding, J.; Casanova, D.; Wu, J. S. Higher Order pi-Conjugated Polycyclic Hydrocarbons with Open-Shell Singlet Ground State: Nonazethrene versus Nonacene. *J. Am. Chem. Soc.* 2016, 138, 10323–10330.
- (8) Mishra, S.; Beyer, D.; Eimre, K.; Liu, J. Z.; Berger, R.; Groning, O.; Pignedoli, C. A.; Mullen, K.; Fasel, R.; Feng, X. L.; Ruffieux, P. Synthesis and Characterization of pi-Extended Triangulene. *J. Am. Chem. Soc.* 2019, 141, 10621–10625.
- (9) Pavliček, N.; Mistry, A.; Majzik, Z.; Moll, N.; Meyer, G.; Fox, D. J.; Gross, L. Synthesis and characterization of triangulene. *Nat. Nanotechnol.* 2017, 12, 308–311.
- (10) Mishra, S.; Xu, K.; Eimre, K.; Komber, H.; Ma, J.; Pignedoli, C. A.; Fasel, R.; Feng, X. L.; Ruffieux, P. Synthesis and characterization of [7] triangulene. *Nanoscale* 2021, 13, 1624–1628.
- (11) Su, J.; Fan, W.; Mutombo, P.; Peng, X. N.; Song, S. T.; Ondracek, M.; Golub, P.; Brabec, J.; Veis, L.; Telychko, M.; Jelinek, P.; Wu, J. S.; Lu, J. On-Surface Synthesis and Characterization of [7] Triangulene Quantum Ring. *Nano Lett.* 2021, 21, 861–867.
- (12) Mishra, S.; Catarina, G.; Wu, F. P.; Ortiz, R.; Jacob, D.; Eimre, K.; Ma, J.; Pignedoli, C. A.; Feng, X. L.; Ruffieux, P.; Fernandez-Rossier, J.; Fasel, R. Observation of fractional edge excitations in nanographene spin chains. *Nature* 2021, 598, 287–292.
- (13) Mishra, S.; Beyer, D.; Eimre, K.; Ortiz, R.; Fernandez-Rossier, J.; Berger, R.; Groening, O.; Pignedoli, C. A.; Fasel, R.; Feng, X. L.; Ruffieux, P. Collective All-Carbon Magnetism in Triangulene Dimers. *Angew. Chem., Int. Ed.* 2020, 59, 12041–12047.
- (14) Su, J.; Telychko, M.; Hu, P.; Macam, G.; Mutombo, P.; Zhang, H. J.; Bao, Y.; Cheng, F.; Huang, Z. Q.; Qiu, Z. Z.; Tan, S. J. R.; Lin, H.; Jelinek, P.; Chuang, F. C.; Wu, J. S.; Lu, J. Atomically precise

- bottom-up synthesis of pi-extended [5]triangulene. Sci. Adv. 2019, 5, No. eaav7717.
- (15) Hieulle, J.; Castro, S.; Friedrich, N.; Vegliante, A.; Lara, F. R.; Sanz, S.; Rey, D.; Corso, M.; Frederiksen, T.; Pascual, J. I.; Pena, D. On-Surface Synthesis and Collective Spin Excitations of a Triangulene-Based Nanostar. *Angew. Chem., Int. Ed.* 2021, 60, 25224–25229.
- (16) da Costa Azevêdo, A. S.; Saraiva-Souza, A.; Meunier, V.; Girao, E. C. Electronic properties of N-rich graphene nano-chevrons. *Phys. Chem. Chem. Phys.* 2021, 23, 13204–13215.
- (17) Kondo, J. Effect of Ordinary Scattering on Exchange Scattering from Magnetic Impurity in Metals. *Phys. Rev.* 1968, 169, 437–440.
- (18) Koch, M.; Ample, F.; Joachim, C.; Grill, L. Voltage-dependent conductance of a single graphene nanoribbon. *Nat. Nanotechnol.* 2012, 7, 713–717.
- (19) Friedrich, N.; Brandimarte, P.; Li, J. C.; Saito, S.; Yamaguchi, S.; Pozo, I.; Pena, D.; Frederiksen, T.; Garcia-Lekue, A.; Sanchez-Portal, D.; Pascual, J. I. Magnetism of Topological Boundary States Induced by Boron Substitution in Graphene Nanoribbons. *Phys. Rev. Lett.* 2020, 125, No. 146801.
- (20) Piskun, I.; Blackwell, R.; Jornet-Somoza, J.; Zhao, F. Z.; Rubio, A.; Louie, S. G.; Fischer, F. R. Covalent C-N Bond Formation through a Surface Catalyzed Thermal Cyclodehydrogenation. *J. Am. Chem. Soc.* 2020, 142, 3696–3700.
- (21) McCurdy, R. D.; Jacobse, P. H.; Piskun, I.; Veber, G. C.; Rizzo, D. J.; Zuzak, R.; Mutlu, Z.; Bokor, J.; Crommie, M. F.; Fischer, F. R. Synergetic Bottom-Up Synthesis of Graphene Nanoribbons by Matrix-Assisted Direct Transfer. J. Am. Chem. Soc. 2021, 143, 4174–4178.
- (22) Konishi, A.; Morinaga, A.; Fukuhara, G.; Nishijima, M.; Mori, T.; Kida, T.; Yasuda, M. 1,8-Diphenyl-9,10-Bis(arylethynyl)-phenanthrenes: Synthesis, Distorted Structure, and Optical Properties. *Chem. Eur. J.* 2018, 24, 6625–6631.
- (23) Hapala, P.; Kichin, G.; Wagner, C.; Tautz, F. S.; Temirov, R.; Jelinek, P. Mechanism of high-resolution STM/AFM imaging with functionalized tips. *Phys. Rev. B* 2014, *90*, No. 085421.
- (24) Wang, X. Y.; Richter, M.; He, Y. Q.; Bjork, J.; Riss, A.; Rajesh, R.; Garnica, M.; Hennersdorf, F.; Weigand, J. J.; Narita, A.; Berger, R.; Feng, X. L.; Auwarter, W.; Barth, J. V.; Palma, C. A.; Mullen, K. Exploration of pyrazine-embedded antiaromatic polycyclic hydrocarbons generated by solution and on-surface azomethine ylide homocoupling. *Nat. Commun.* 2017, 8, No. 1948.
- (25) Cai, J. M.; Ruffieux, P.; Jaafar, R.; Bieri, M.; Braun, T.; Blankenburg, S.; Muoth, M.; Seitsonen, A. P.; Saleh, M.; Feng, X. L.; Müllen, K.; Fasel, R. Atomically precise bottom-up fabrication of graphene nanoribbons. *Nature* 2010, 466, 470–473.
- (26) Jacobse, P. H.; McCurdy, R. D.; Jiang, J. W.; Rizzo, D. J.; Veber, G.; Butler, P.; Zuzak, R.; Louie, S. G.; Fischer, F. R.; Crommie, M. F. Bottom-up Assembly of Nanoporous Graphene with Emergent Electronic States. *J. Am. Chem. Soc.* 2020, 142, 13507–13514.
- (27) Frank, S.; Jacob, D. Orbital signatures of Fano-Kondo line shapes in STM adatom spectroscopy. *Phys. Rev. B* 2015, 92, No. 235127.
- (28) Frota, H. O. Shape of the Kondo Resonance. *Phys. Rev. B* 1992, 45, 1096–1099.
- (29) Madhavan, V.; Chen, W.; Jamneala, T.; Crommie, M. F.; Wingreen, N. S. Tunneling into a single magnetic atom: Spectroscopic evidence of the Kondo resonance. *Science* 1998, 280, 567–569.
- (30) Li, J. T.; Schneider, W. D.; Berndt, R.; Delley, B. Kondo scattering observed at a single magnetic impurity. *Phys. Rev. Lett.* 1998, 80, 2893–2896.
- (31) Ternes, M.; Heinrich, A. J.; Schneider, W. D. Spectroscopic manifestations of the Kondo effect on single adatoms. *J. Phys. Condens. Mat.* 2009, 21, No. 053001.
- (32) DiLullo, A.; Chang, S. H.; Baadji, N.; Clark, K.; Klockner, J. P.; Prosenc, M. H.; Sanvito, S.; Wiesendanger, R.; Hoffmann, G.; Hla, S. W. Molecular Kondo Chain. *Nano Lett.* 2012, 12, 3174–3179.

- (33) Li, J. C.; Sanz, S.; Corso, M.; Choi, D. J.; Pena, D.; Frederiksen, T.; Pascual, J. I. Single spin localization and manipulation in graphene open-shell nanostructures. *Nat. Commun.* 2019, *10*, No. 200.
- (34) Sun, Q.; Mateo, L. M.; Robles, R.; Lorente, N.; Ruffieux, P.; Bottari, G.; Torres, T.; Fasel, R. Bottom-up Fabrication and Atomic-Scale Characterization of Triply Linked, Laterally pi-Extended Porphyrin Nanotapes. *Angew. Chem., Int. Ed. Engl.* 2021, 60, 16208–16214.
- (35) Wang, T.; Berdonces-Layunta, A.; Friedrich, N.; Vilas-Varela, M.; Calupitan, J. P.; Pascual, J. I.; Pena, D.; Casanova, D.; Corso, M.; de Oteyza, D. G. Aza-Triangulene: On-Surface Synthesis and Electronic and Magnetic Properties. J. Am. Chem. Soc. 2022, 144, 4522–4529.
- (36) Nagaoka, K.; Jamneala, T.; Grobis, M.; Crommie, M. F. Temperature dependence of a single Kondo impurity. *Phys. Rev. Lett.* 2002, 88, No. 077205.
- (37) Tsukahara, N.; Shiraki, S.; Itou, S.; Ohta, N.; Takagi, N.; Kawai, M. Evolution of Kondo Resonance from a Single Impurity Molecule to the Two-Dimensional Lattice. *Phys. Rev. Lett.* 2011, 106, No. 187201
- (38) Simon, P.; Lopez, R.; Oreg, Y. Ruderman-Kittel-Kasuya-Yosida and magnetic-field interactions in coupled Kondo quantum dots. *Phys. Rev. Lett.* 2005, 94, No. 086602.
- (39) Iancu, V.; Deshpande, A.; Hla, S. W. Manipulating Kondo temperature via single molecule switching. *Nano Lett.* 2006, 6, 820–823
- (40) da Silva, L. G. G. V. D.; Tiago, M. L.; Ulloa, S. E.; Reboredo, F. A.; Dagotto, E. Many-body electronic structure and Kondo properties of cobalt-porphyrin molecules. *Phys. Rev. B* 2009, *80*, No. 155443.
- (41) Perera, U. G. E.; Kulik, H. J.; Iancu, V.; da Silva, L. G. G. V. D.; Ulloa, S. E.; Marzari, N.; Hla, S. W. Spatially Extended Kondo State in Magnetic Molecules Induced by Interfacial Charge Transfer. *Phys. Rev. Lett.* 2010, 105, No. 106601.
- (42) Wang, W. H.; Pang, R.; Kuang, G. W.; Shi, X. Q.; Shang, X. S.; Liu, P. N.; Lin, N. Intramolecularly resolved Kondo resonance of high-spin Fe(II)-porphyrin adsorbed on Au(111). *Phys. Rev. B* 2015, 91, No. 045440.
- (43) Komeda, T.; Isshiki, H.; Liu, J.; Katoh, K.; Yamashita, M. Variation of Kondo Temperature Induced by Molecule-Substrate Decoupling in Film Formation of Bis (phthalocyaninato)terbium(III) Molecules on Au(111). ACS Nano 2014, 8, 4866–4875.
- (44) Stoner, E. C. Collective electron ferromagnetism. Proc. R. Soc. Lon. Ser. A 1938, 165, 372-414.
- (45) Lawrence, J.; Brandimarte, P.; Berdonces-Layunta, A.; Mohammed, M. S. G.; Grewal, A.; Leon, C. C.; Sanchez-Portal, D.; de Oteyza, D. G. Probing the Magnetism of Topological End States in 5-Armchair Graphene Nanoribbons. *ACS Nano* 2020, *14*, 4499–4508.
- (46) CrysAlisPro, 1.171.40.82a, 1.171.41.116aOxford Diffraction/Agilent Technologies UK Ltd.: Oxford, UK, 2015.
- (47) Giannozzi, P.; Baroni, S.; Bonini, N.; Calandra, M.; Car, R.; Cavazzoni, C.; Ceresoli, D.; Chiarotti, G. L.; Cococcioni, M.; Dabo, I.; Dal Corso, A.; de Gironcoli, S.; Fabris, S.; Fratesi, G.; Gebauer, R.; Gerstmann, U.; Gougoussis, C.; Kokalj, A.; Lazzeri, M.; Martin-Samos, L.; Marzari, N.; Mauri, F.; Mazzarello, R.; Paolini, S.; Pasquarello, A.; Paulatto, L.; Sbraccia, C.; Scandolo, S.; Sclauzero, G.; Seitsonen, A. P.; Smogunov, A.; Umari, P.; Wentzcovitch, R. M. QUANTUM ESPRESSO: a modular and open-source software project for quantum simulations of materials. *J. Phys. Condens. Mat.* 2009, 21, No. 395502.

☐ Recommended by ACS

Manipulation of Spin Polarization in Boron-Substituted Graphene Nanoribbons

Kewei Sun, Shigeki Kawai, et al.

JUNE 22, 2022

ACS NANO

READ 🗹

Gate-Tunable Proximity Effects in Graphene on Layered Magnetic Insulators

Chun-Chih Tseng, Matthew Yankowitz, et al.

OCTOBER 24, 2022

NANO LETTERS

READ ☑

Accelerated Ultrafast Magnetization Dynamics at Graphene/CoGd Interfaces

Sucheta Mondal, Jeffrey Bokor, et al.

JUNE 13, 2022

ACS NANO

READ ☑

Graphene Lattices with Embedded Transition-Metal Atoms and Tunable Magnetic Anisotropy Energy: Implications for Spintronic Devices

Rostislav Langer, Piotr Błoński, et al.

JANUARY 18, 2022

ACS APPLIED NANO MATERIALS

READ ☑

Get More Suggestions >